

## Article

# Fabrication of High-Performance Asymmetric Supercapacitor Consists of Nickel Oxide and Activated Carbon (NiO//AC)

Rajangam Vinodh <sup>1,†</sup>, Rajendran Suresh Babu <sup>2,\*</sup>, Raji Atchudan <sup>3,†</sup>, Hee-Je Kim <sup>4</sup>, Moonsuk Yi <sup>1,\*</sup>, Leandro Marques Samyn <sup>2</sup> and Ana Lucia Ferreira de Barros <sup>2</sup>

<sup>1</sup> Department of Electronics Engineering, Pusan National University, Busan 46241, Korea; vinoth6482@gmail.com

<sup>2</sup> Laboratory of Experimental and Applied Physics, Centro Federal de Educação Tecnológica Celso Suckow da Fonseca, Av. Maracanã Campus 229, Rio de Janeiro 20271-110, Brazil; leandro.samyn@cefet-rj.br (L.M.S.); ana.barros@cefet-rj.br (A.L.F.d.B.)

<sup>3</sup> Department of Chemical Engineering, Yeungnam University, Gyeongsan 38541, Korea; atchudanr@yu.ac.kr

<sup>4</sup> Department of Electrical and Computer Engineering, Pusan National University, Busan 46241, Korea; heeje@pusan.ac.kr

\* Correspondence: ryesbabu@gmail.com (R.S.B.); msyi@pusan.ac.kr (M.Y.)

† These authors contributed equally to this work.

**Abstract:** Exploring faster, safer, and more efficient energy storage devices will motivate scientists to develop novel energy storage products with high performance. Herein, we report porous NiO nanoparticles have been prepared by a simple hydrothermal method with CTAB and laboratory tissue paper as a template followed by calcination at three different temperatures (300, 500, and 700 °C). The electrochemical characteristics of the prepared materials were examined in a three-electrode cell configuration using aqueous potassium hydroxide (2.0 M KOH) electrolyte. The NiO-300 electrode displayed the supreme capacitance of 568.7 F g<sup>-1</sup> at 0.5 A g<sup>-1</sup>. The fascinating NiO morphology demonstrates a crucial part in offering simple ion transport, shortening electron, and ion passage channels and rich energetic spots for electrochemical reactions. Finally, the asymmetric supercapacitor (ASC), NiO//AC was constructed using positive and negative electrode materials of NiO-300 and activated carbon (AC), respectively. The assembled ASC displayed excellent supercapacitive performance with a high specific energy (52.4 Wh kg<sup>-1</sup>), specific power (800 W kg<sup>-1</sup>), and remarkable cycle life. After quick charging (25 s), such supercapacitors in the series will illuminate the light emitting diode for an extended time, suggesting improvements in energy storage, scalable integrated applications, and ensuring business efficacy. This work will lead to a new generation of high-performance ASCs to portable electronic displays and electric automobiles.

**Keywords:** energy storage; hydrothermal; nanoflakes; nickel oxide; tissue paper; supercapacitors



**Citation:** Vinodh, R.; Babu, R.S.; Atchudan, R.; Kim, H.-J.; Yi, M.; Samyn, L.M.; de Barros, A.L.F. Fabrication of High-Performance Asymmetric Supercapacitor Consists of Nickel Oxide and Activated Carbon (NiO//AC). *Catalysts* **2022**, *12*, 375. <https://doi.org/10.3390/catal12040375>

Academic Editor: Yat Li

Received: 5 March 2022

Accepted: 25 March 2022

Published: 27 March 2022

**Publisher's Note:** MDPI stays neutral with regard to jurisdictional claims in published maps and institutional affiliations.



**Copyright:** © 2022 by the authors. Licensee MDPI, Basel, Switzerland. This article is an open access article distributed under the terms and conditions of the Creative Commons Attribution (CC BY) license (<https://creativecommons.org/licenses/by/4.0/>).

## 1. Introduction

As fossil fuel consumption and environmental concerns increase, scientists and technologists are focusing on the development of renewable energy sources. To maximize usage of the electricity provided by such intermediate renewable sources, efficient energy storage technologies are required. As a result, the growth of high-efficiency energy storing devices is paramount [1–3]. Electrochemical capacitors (also termed supercapacitors) are of great interest owing to their extreme specific power, outstanding extended durability, and quick charging–discharging rate [4,5]. According to their mechanism of energy storage, supercapacitors (SCs) can be divided into two main types. The electric double-layer capacitor (EDLC) is one type of capacitor that stores electrical energy by accumulating electric charges at the electrode and electrolyte interface [6]. The most employed materials for EDLC electrodes are high specific surface area carbon-based materials such as porous carbon [7–9], carbon fibers (CFs) [10,11], carbon nanotubes (CNTs) [12], and graphene [13].

The pseudo-capacitor (PC), on the other hand, is another type of capacitor derived from Faradaic (redox) reactions at the electrode–electrolyte interface, which has attracted much consideration due to its significantly higher capacitance [14–16]. The pseudocapacitor is mainly based on conducting polymers [17–20], metal hexacyanoferrates [17,18], and metal oxides [21,22].

Recently, a lot of research on transition metal oxides (TMOs) and hydroxides—for example, RuO<sub>2</sub>, MnO<sub>2</sub>, Co<sub>2</sub>O<sub>3</sub>, NiO, CuO, Ni(OH)<sub>2</sub>, and others—has been reported as the most used pseudocapacitive materials for high energy density because of their desirable theoretical capacitance. Among them, RuO<sub>2</sub> has gained more attention owing to its superior capacitance, long cut-off voltage, and outstanding cyclic durability [23,24]. However, the high price of RuO<sub>2</sub> prevents its practical application despite its excellent capacitive performance. Therefore, many investigators in this area are looking for substitute candidate materials such as NiO, Co<sub>2</sub>O<sub>3</sub>, and MnO<sub>2</sub> [25–30]. MnO<sub>2</sub> has attracted great attention due to its abundance in earth's crust, excellent electrochemical stability, and extraordinary specific capacitance. Regrettably, at high scan rates, MnO<sub>2</sub> fails to maintain the required capacitance when charging–discharging [31,32]. Among these electrode materials, nickel oxide (NiO) seems to be a capable substitute owing to its huge theoretical specific capacitance value of 2573 F g<sup>−1</sup>, low production price, and ecological impression [33]. Nevertheless, its comparatively inferior electrical conductivity and short accessibility surface areas generally lead to poor reversibility and restricted capacitance during the charge and discharge process in experimentation. A better resolution to this tricky situation is to enlarge their active surface areas by transforming objects from bulk systems into porous/hollow architectures. Very recently, scientific communities have produced NiO with different structural morphology and surface textures, comprising nanoflowers, nanoplates, nanoparticles, and nanoflakes [34–37].

In this present investigation, we explore a simple and consistent technique to synthesize NiO electrode materials with excellent electrochemical performance. NiO nanoparticles anchored on flakes have been synthesized by a simple hydrothermal method with CTAB and laboratory tissue paper as the template and followed by calcination. The electrochemical characteristics of the synthesized NiO materials were examined in a three-compartment cell set-up in aqueous 2.0 M KOH. The prepared NiO-300 electrode displayed the supreme specific capacitance of 568.7 F g<sup>−1</sup> at 0.5 A g<sup>−1</sup> and excellent rate capability. Moreover, the ASC (NiO-300//AC) was constructed using positive and negative electrode materials of NiO-300 and AC, respectively. The fabricated ASC displayed excellent supercapacitive behavior with a high energy density, power density, and exceptional cyclability.

## 2. Experimental

### 2.1. Chemicals

Nickel nitrate Ni(NO<sub>3</sub>)<sub>2</sub>, cetyltrimethylammonium bromide (CTAB), and potassium hydroxide (KOH) were obtained from Sigma Aldrich, St. Louis, MI, USA. Nickel foam was also procured from Sigma Aldrich. The cellulose filter paper (papel Filtro Qualy) was procured from J Prolab Ind. E. Com. De Prod. P/Lab. LTDA. The tissue papers were purchased from the local market, Rio de Janeiro, Brazil (Melhoramentos CMPC LTDA). All other chemicals were of analytical grade and used as received without further purification. In all experiments, double distilled water was used.

### 2.2. Synthesis of NiO Nanoparticles

All the reagents were used as received. The collected fresh tissue papers (TPs) were torn into a tiny pieces. In a typical synthesis procedure of the porous nickel oxide, 0.5811 g of nickel nitrate was kept in a beaker (100 mL) along with 10 mL deionized water at ambient temperature while magnetic stirring. Then, 0.3645 g of CTAB was dispersed in 40 mL deionized water and slowly added into the above solution in stirring condition. Subsequently, previously torn TPs (100 g) were put into the above reaction mixture. Finally, the prepared solution was moved into the Teflon-lined stainless steel (SS) autoclave. The

autoclave was maintained at 120 °C for 12 h in the muffle furnace. After the reaction completed, the autoclave was permitted to cool at ambient temperature. The resultant material was collected and rinsed with copious amount of DI water and ethanol to eliminate the unreacted materials/solvents. The cleaned materials were dehydrated in a vacuum oven at 80 °C overnight. Lastly, the desiccated samples were smashed and sintered at three various temperatures (300, 500, and 700 °C) for 2 h under air atmosphere. The final derived materials were named NiO-300, NiO-500, and NiO-700 according to their calcination temperature. The pictorial representation of the preparation method was illustrated in Figure 1.

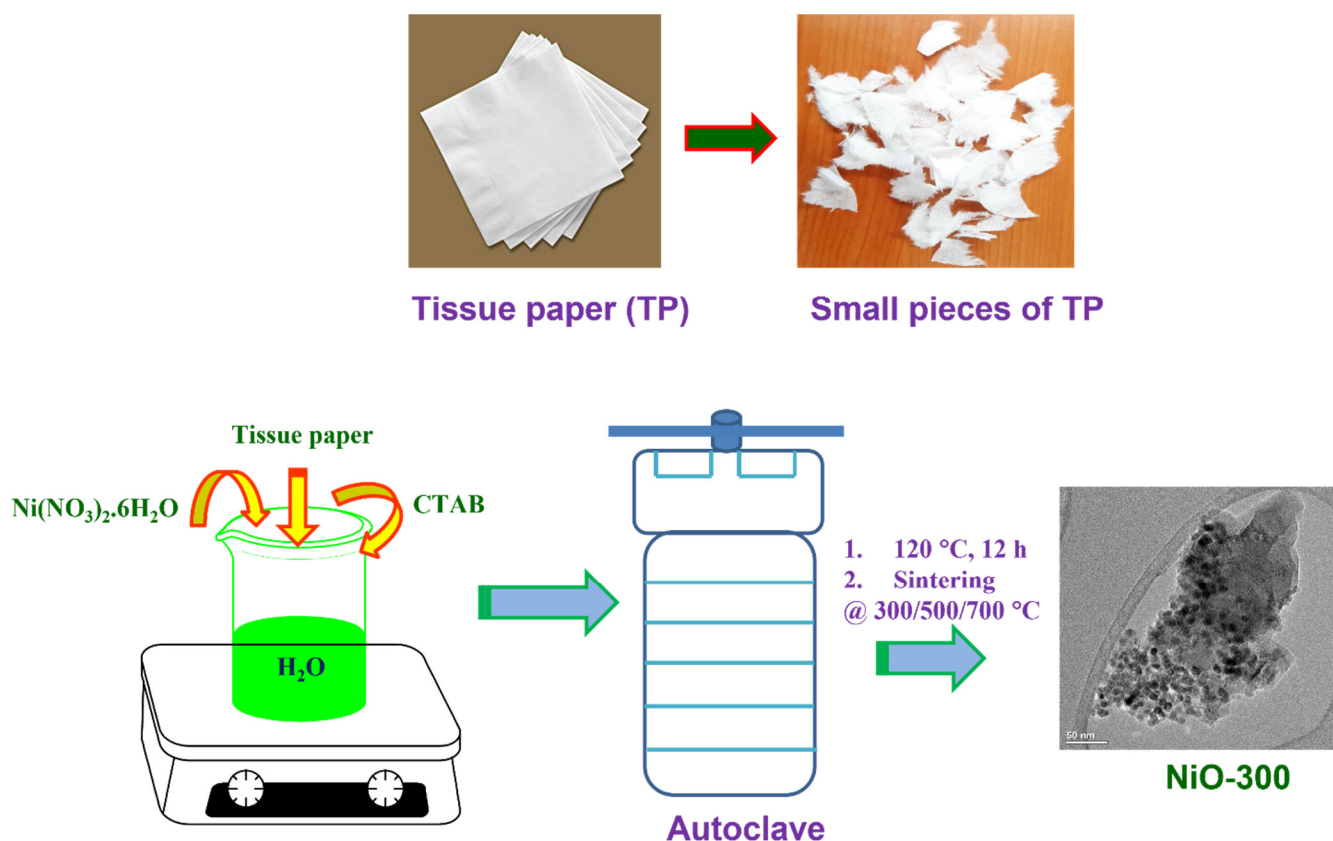


**Figure 1.** Pictorial representation of the reaction protocol of nickel oxide nanoparticles.

### 2.3. Characterization Techniques

X-ray diffraction (XRD) pattern was applied to explore the phase purity and crystal structure of the obtained materials with Cu-K $\alpha$  radiation (Rigaku;  $\lambda = 0.1541$  nm) between  $2\theta$  value of 30 and 80°. The surface morphology and topography of the prepared materials was examined through field-emission scanning electron microscope (FE-SEM: Hitachi S-2400, Tokyo, Japan) and transmission electron microscope (TEM: JEOL, Tokyo, Japan), respectively.

### 2.4. Electrochemical Measurements

To explore the electrochemical characteristics of the prepared electrode materials, cyclic voltammetry (CV), galvanostatic charge–discharge (GCD), and electrochemical impedance spectroscopy (EIS) were examined by using IVIUM electrochemical instrument. A three-electrode cell set up was used for the electrochemical measurements with an aqueous KOH (2.0 M) electrolyte at ambient temperature. The Pt mesh and Ag/AgCl were applied as the auxiliary and reference electrodes, respectively. The fabrication of working electrode required the following, 80% of active material (NiO-300, NiO-500, and NiO-700), 10% of conductive material (carbon black), and 10% of binder material (polyvinylidene fluoride)

dissolved with N-methyl pyrrolidone as a solvent. The above materials were well mixed to make a thick slurry which was coated on pretreated Ni foam ( $1 \times 1 \text{ cm}^2$ ) with spatula and desiccated for 24 h at  $120 \text{ }^\circ\text{C}$ . The average mass of the active material was found to be 4.0 mg. Based on Equation (1), the specific capacitance ( $C_s$ ) of the NiO electrode samples were estimated from the discharge curve of GCD [10,22].

$$C_s = It/m\Delta V \quad (1)$$

where  $I$  signifies the given current in amps,  $m$  represents the mass of the active sample in gram,  $\Delta V$  designates the cut-off range ( $E$ ), and  $t$  designates the discharging time in seconds.

### 2.5. Fabrication of ASC Device

The fabrication of ASC device was integrating the cathode (NiO-300) and the anode (AC) is separated using cellulose filter paper (immersed overnight in 2.0 M KOH electrolyte) and subsequently enfolded with insulation tape. The anode and cathode had an analogous geometric surface area ( $1 \times 1 \text{ cm}^2$  size). To attain the weight ratio of NiO and AC electrode materials, we had to apply the equation of charge balance ( $q_+ = q_-$ ). The weight of the NiO-300 and AC electrodes were altered based on the following Equation (2) [10,22].

$$m^+/m^- = C^- \times V^-/C^+ \times V^+ \quad (2)$$

where  $C$  indicates the specific capacitance (obtained via three-electrode configuration),  $m$  signifies the weight of the electrode materials, and  $V$  represents the cut-off region for the cathode and anode.

Based on the Equation (1), the weight ratio of  $\sim 1$  was fixed for the charge balance between the electrodes of NiO and AC in the ASC device. To find the electrochemical behavior at the voltage ranging between 0 and 1.6 V, the crucial constraints of the ASC device, for example specific capacitance, energy density ( $E_D$ ;  $\text{Wh kg}^{-1}$ ), and power density ( $P_D$ ;  $\text{W kg}^{-1}$ ) were attained by the subsequent equations [38,39]:

$$C_D = 2 \times I\Delta t/m\Delta V \quad (3)$$

$$E_D = C_D\Delta V^2/8 \times 3.6 \quad (4)$$

$$P_D = E_D \times 3600/\Delta t \quad (5)$$

Electrochemical impedance spectroscopy (EIS) was examined at formal potential of the working electrodes by sweeping the frequency from 0.1 Hz to 100 kHz at an amplitude of 5 mV.

## 3. Results and Discussion

The crystalline nature and physical information of the prepared NiO materials were explored by XRD. Figure 2a depicts the sharp intense peak of NiO nanoflakes and it clearly illustrates the crystallinity of the prepared materials. XRD pattern exhibits four major diffraction peaks at  $2\theta$  value of  $36.9^\circ$ ,  $43.4^\circ$ ,  $63.2^\circ$ , and  $73.9^\circ$  matches with (111), (200), (220), and (311) planes, correspondingly. The above results are well coincided with the COD data of NiO 96-101-0096 [40]. The obvious differences were observed from one material to another material either due to the noise of the instrument or some impurities that would have got embedded in the sample during the operation of the instrument. Furthermore, the intensity of diffraction peaks gradually increased with increasing the calcination temperatures up to  $500 \text{ }^\circ\text{C}$  (NiO-500). For the sample calcined at  $700 \text{ }^\circ\text{C}$  (NiO-700), the diffraction peaks decreased and even some of the peaks are fully vanished.

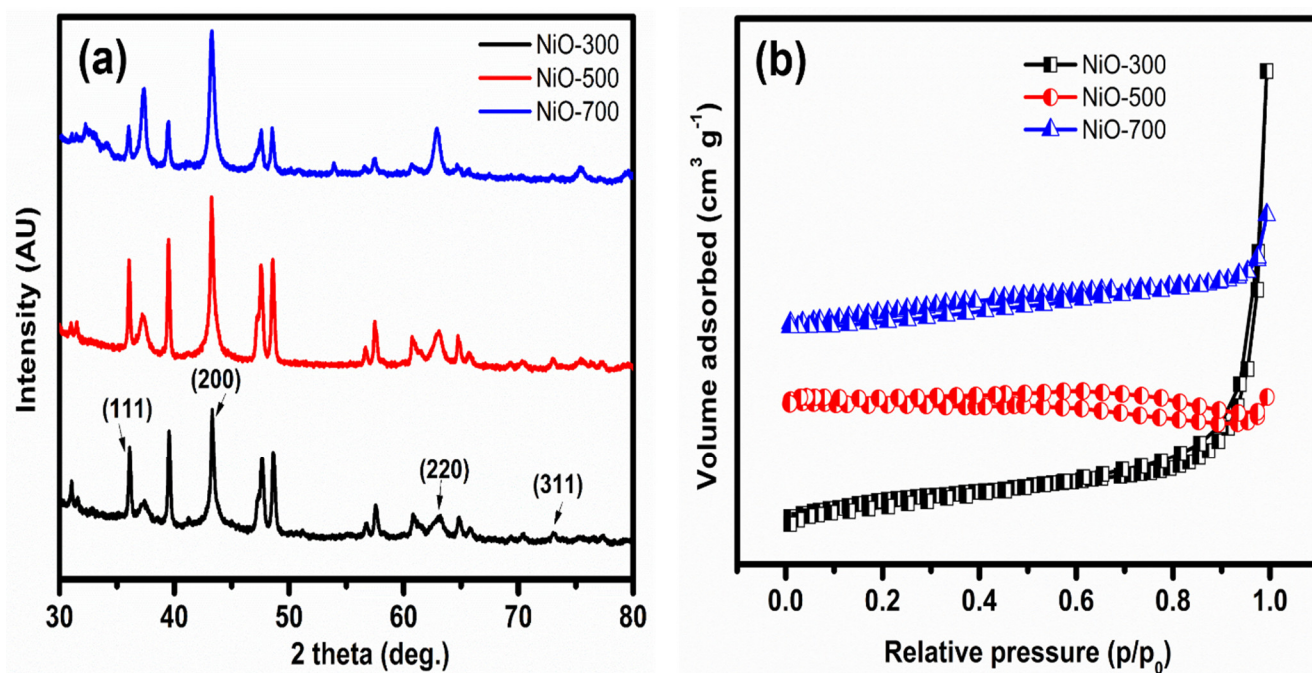
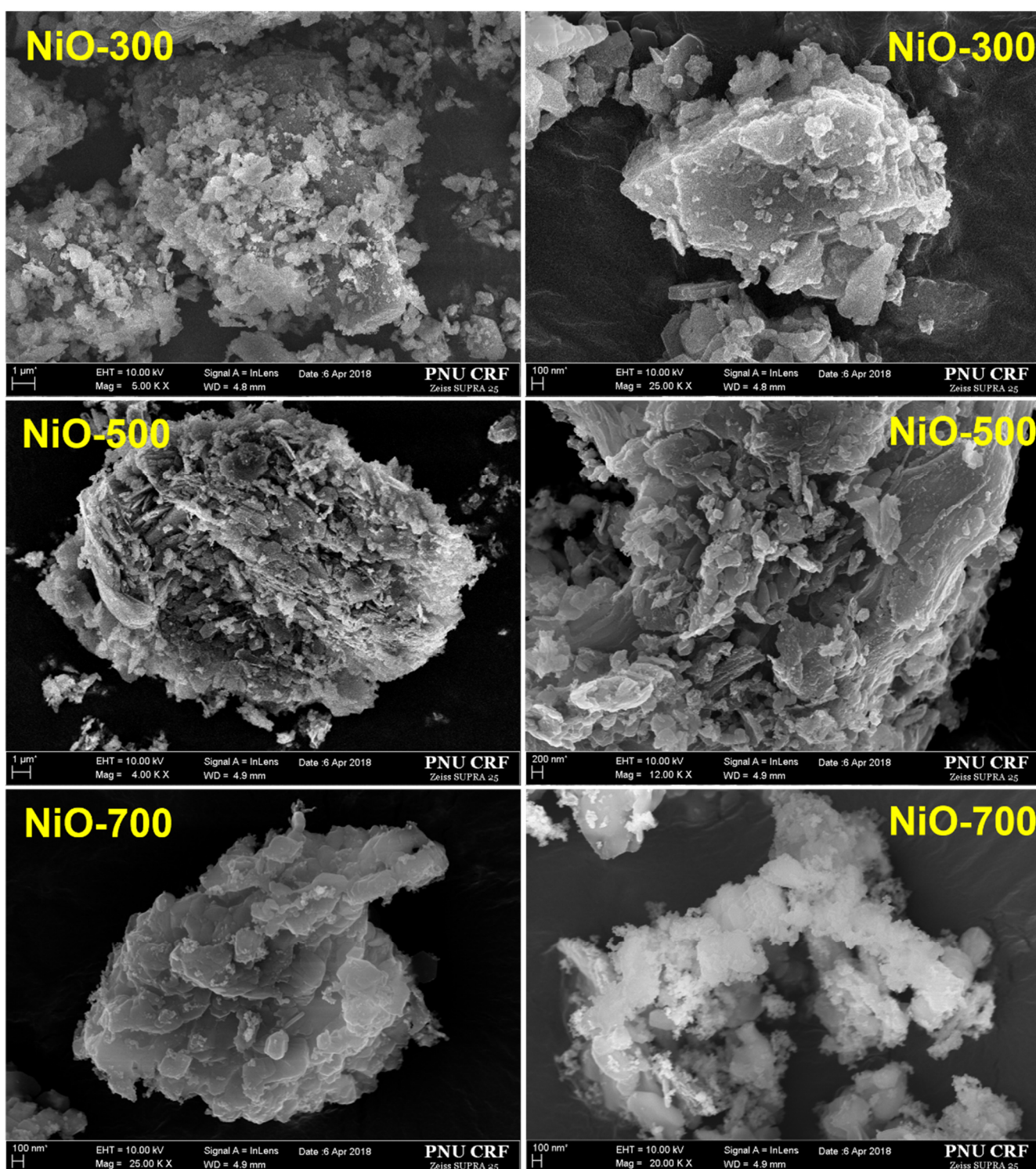


Figure 2. (a) XRD and (b) N<sub>2</sub> sorption isotherms of NiO materials prepared at three different temperatures.

The nitrogen adsorption–desorption isotherms for all the prepared materials were carried out to characterize their BET surface area and porosity. Based on the adsorption–desorption curves shown in Figure 2b, NiO-300 exhibits type II isotherm whereas NiO-500 and NiO-700 exhibit type-III isotherm. At initial and mid relative pressures ( $p/p_0 = 0.1$ ), all three materials exhibited a tiny and sharp increase in the volume of nitrogen adsorption indicates the existence of micropores, and mesopores respectively. Whereas steep enhancement was observed at high relative pressure of  $p/p_0 = 1$  illustrates the presence of macropores. The existence of hierarchical pores (i.e., micro-, meso-, and macropores) is one of the beneficial parameters for supercapacitor applications. Because it will allow the passage of electron at electrode–electrolyte interfaces. The maximum surface area was found to be  $48 \text{ m}^2 \text{ g}^{-1}$  for NiO-300, whereas 32 and  $27 \text{ m}^2 \text{ g}^{-1}$  obtained for NiO-500 and NiO-700, respectively.

Figure 3 represents the FE-SEM pictures of the NiO materials prepared at different temperatures. All three materials exhibit flake-like morphology with tiny nanoparticles, with a porous open channel within the flake morphology. NiO-300 and NiO-500 materials possess large number of flake-like structures with minimal number of nanoparticles. While FE-SEM images of NiO-700 displayed the aggregates of fine nanoparticles completely agglomerated on the flakes. The porous architecture developed inside the flake-like morphology of the NiO is owing to the decomposition of chemically bonded groups and the evaporation of water molecules. Furthermore, the obtained nanoparticles along with flakes are well-organized and the pores between nanoparticles could serve as effective pathways for the electrolyte throughout redox process. Therefore, almost all of the nanoparticles are extremely available to the electrolyte, leading to an extraordinary charge–discharge capacity [41,42].



**Figure 3.** FE-SEM photographs of the obtained NiO materials with different calcination temperatures.

The detailed morphological characteristics of the synthesized materials were established further by TEM performance. Figure 4 exhibits the characteristic TEM pictures of NiO-300, NiO-500, and NiO-800 samples. The obtained TEM pictures are completely dependable with the FE-SEM outcomes (Figure 3). A well-organized channel with particularly small pores was observed in NiO-300, where smaller NiO particles can pack closer to each other, developing a narrow channel within the flake-like structure. When the temperature increases (NiO-500 and NiO-700), the growth of the NiO crystallite size, which formed

larger and rougher particles, made the close packing of the NiO difficult. Therefore, large architecture was formed within the flake structure [43].

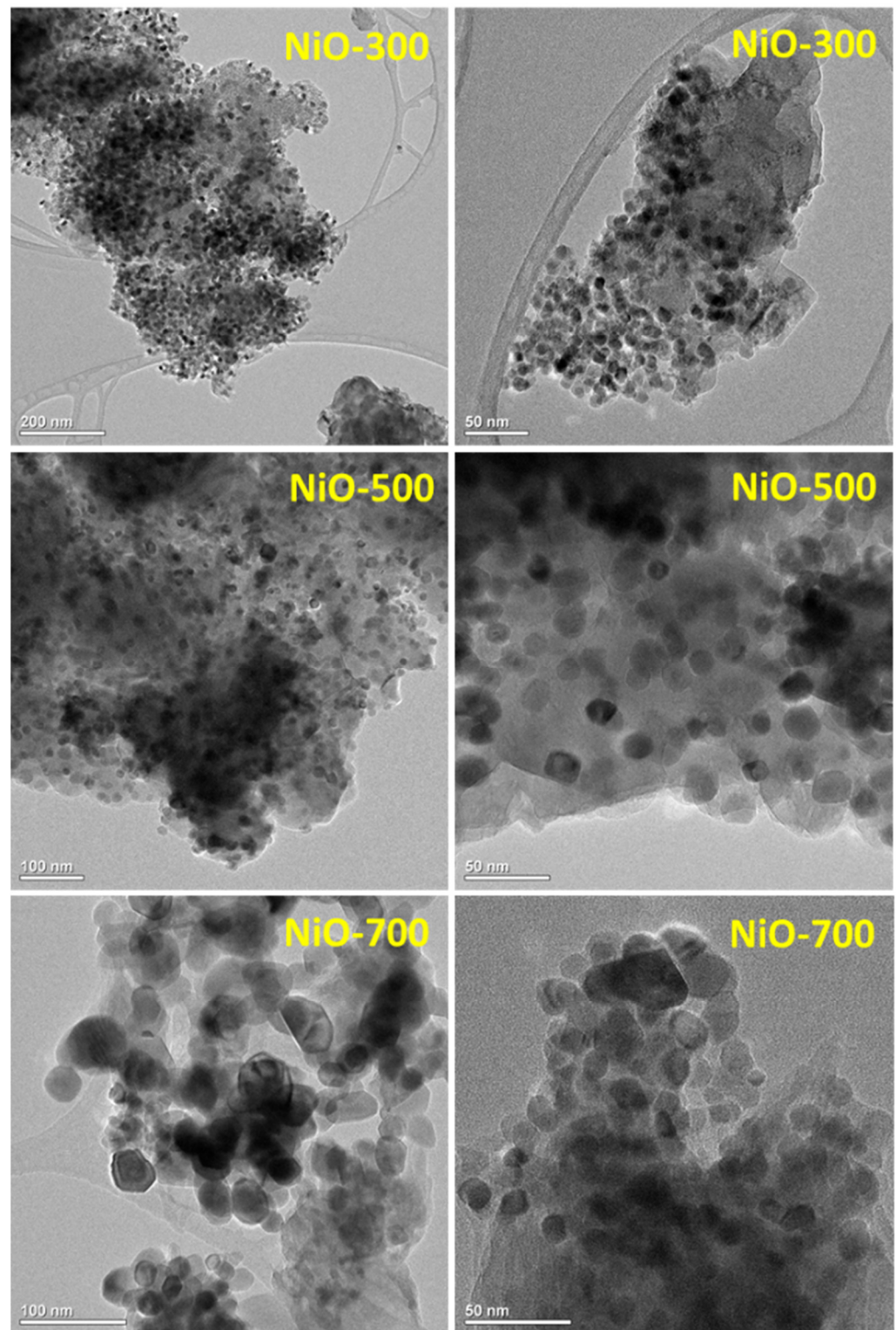


**Figure 4.** TEM images of the different NiO materials.

The electrochemical characterization, such as CV and GCD methods, was employed to calculate the supercapacitive properties of as-prepared NiO materials in 2.0 M KOH aqueous solution. CV is an appropriate technique to describe the capacitive performance of as-prepared electrode materials. Figure 5a illustrates the comparative CV curves of the three different NiO samples (NiO-300, NiO-500, and NiO-700) in a three-electrode set up at sweep rate of  $10 \text{ mV s}^{-1}$  with cut-off region from 0 to 0.6 V versus Ag/AgCl reference electrode. During the sweeps, the redox peaks are obtained, in which nickel oxide is oxidized to nickel oxyhydroxide (NiO/NiOOH) during the cycling in aqueous solutions KOH electrolyte. Hence, the capacitance is primarily coming from the redox reaction (Faradaic reaction) of  $\text{Ni}^{2+}/\text{Ni}^{3+}$  obtained at the electrode surface. The shape of the CVs is close to a well-defined redox peak, which is distinguished as that of pseudocapacitance behavior. In the KOH electrolyte, the general electrochemical reaction mechanism for NiO electrode is

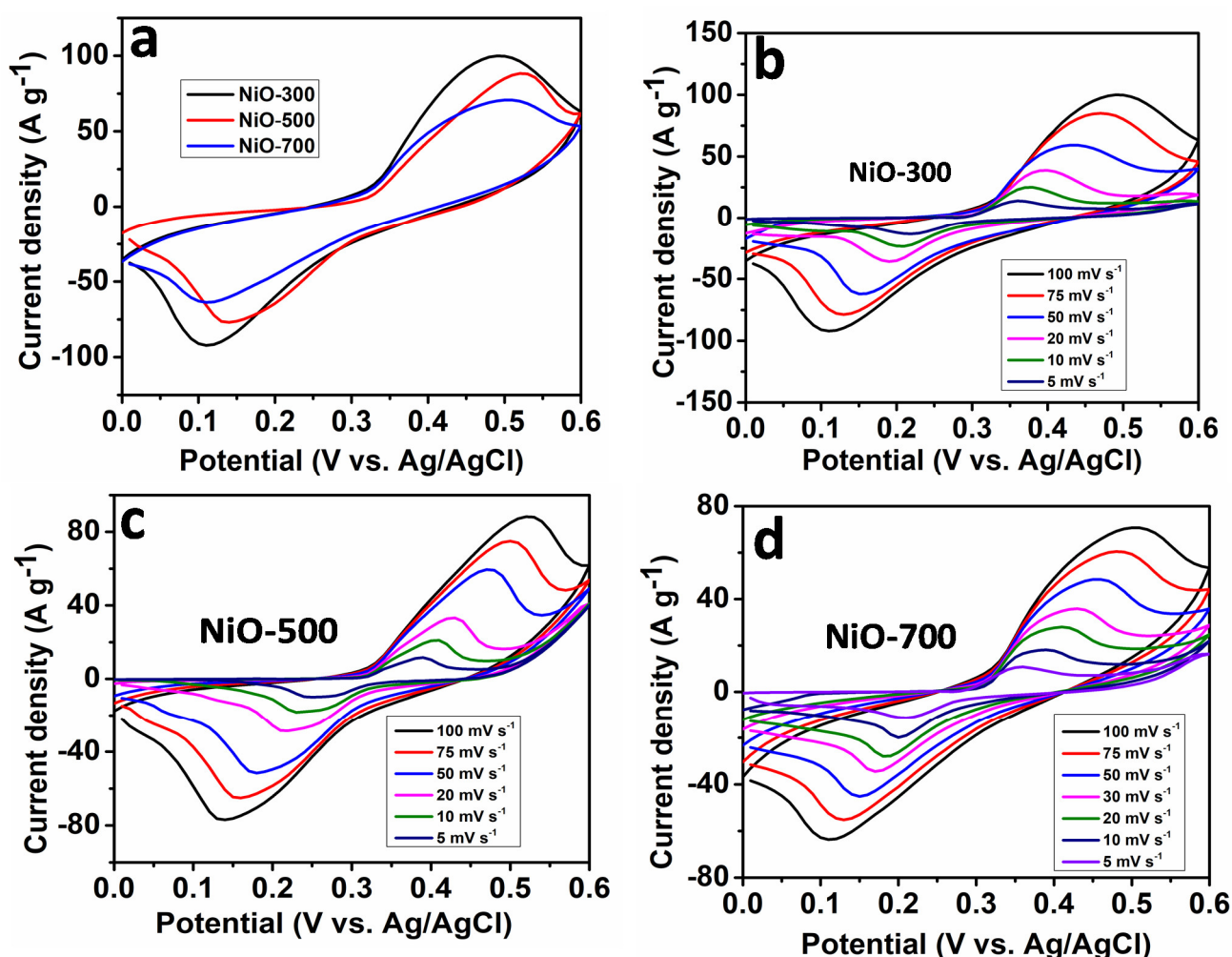
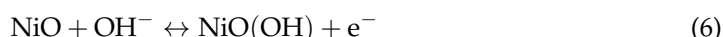


**Figure 5.** (a) Comparative CV profile of three different NiO electrodes; (b–d) CV profiles of NiO-300, NiO-500, and NiO-700 at various sweep rates, respectively.

Among the three different NiO electrode materials, evidently NiO-300 showed an enhanced current response than that of NiO-500 and NiO-700 electrodes indicating the higher surface area and porous nature, which makes it easier for ion diffusion throughout the material surface and the charge transfer reaction. Figure 5b–d illustrates the CV profiles of NiO-300, NiO-500, and NiO-700, respectively with varying the sweep rate at 5, 10, 20, 50, 75,  $100 \text{ mV s}^{-1}$  with a cut-off region from 0 to 0.6 V in a 2.0 M KOH electrolyte. The anodic

peak current density and cathodic peak current density increases linearly with square-root of the sweep rate in all three voltammograms, demonstrating that the corresponding reduction and oxidation reaction is a diffusion-controlled process [44].

Figure 6a illustrates typical GCD curves of as-prepared NiO electrodes estimated an applied current density of  $0.5 \text{ A g}^{-1}$ . Compared with the NiO-300 electrode, NiO-500 and NiO-700 electrodes have slower charge kinetics. The rapid charge–discharge characteristics of NiO-300 were attributed to the more pores and well-organized architecture sites with a reduced number of margins that allow for free access during the charge and discharge cycles. The long discharging time of the GCD curve was observed for NiO-300, which was further established by the outcomes attained from the voltammogram plots (Figure 5a). Figure 6b–d illustrates the GCD curves of three different NiO electrode materials with various densities of current ranging between  $0.5$  and  $20 \text{ A g}^{-1}$  within the potential window range between  $0.0$  and  $0.40 \text{ V vs. Ag/AgCl}$ . The GCD profiles are approximately symmetric and a pair of charge–discharge plateau responses that were associated to the indication of oxidation and reduction process of NiO. The NiO-300 electrode shows 68% of the columbic efficiency in the initial cycles, whereas the NiO-500 and NiO-700 electrodes display 52% and 48%, respectively. The electrode materials signify moderate columbic efficiencies owing to electrochemical reactions and excellent electric conductivity. Furthermore, for Faradaic redox processes, all three electrode materials have battery-like properties [10,14]. The gravimetric capacitances of all the three different NiO electrodes are estimated from the discharge profiles and are shown in Figure 6e. It was clear that NiO-300 establishes the higher discharging time, illustrating the high specific capacitance of  $568.7 \text{ F g}^{-1}$  at  $0.5 \text{ A g}^{-1}$ . When the current density increases progressively, the specific capacitance decreases, which might be rate-limited kinetics by electrolyte ion-diffusion into the active materials. In addition, the GCD consequences are well-matched with the obtained CV characteristics.

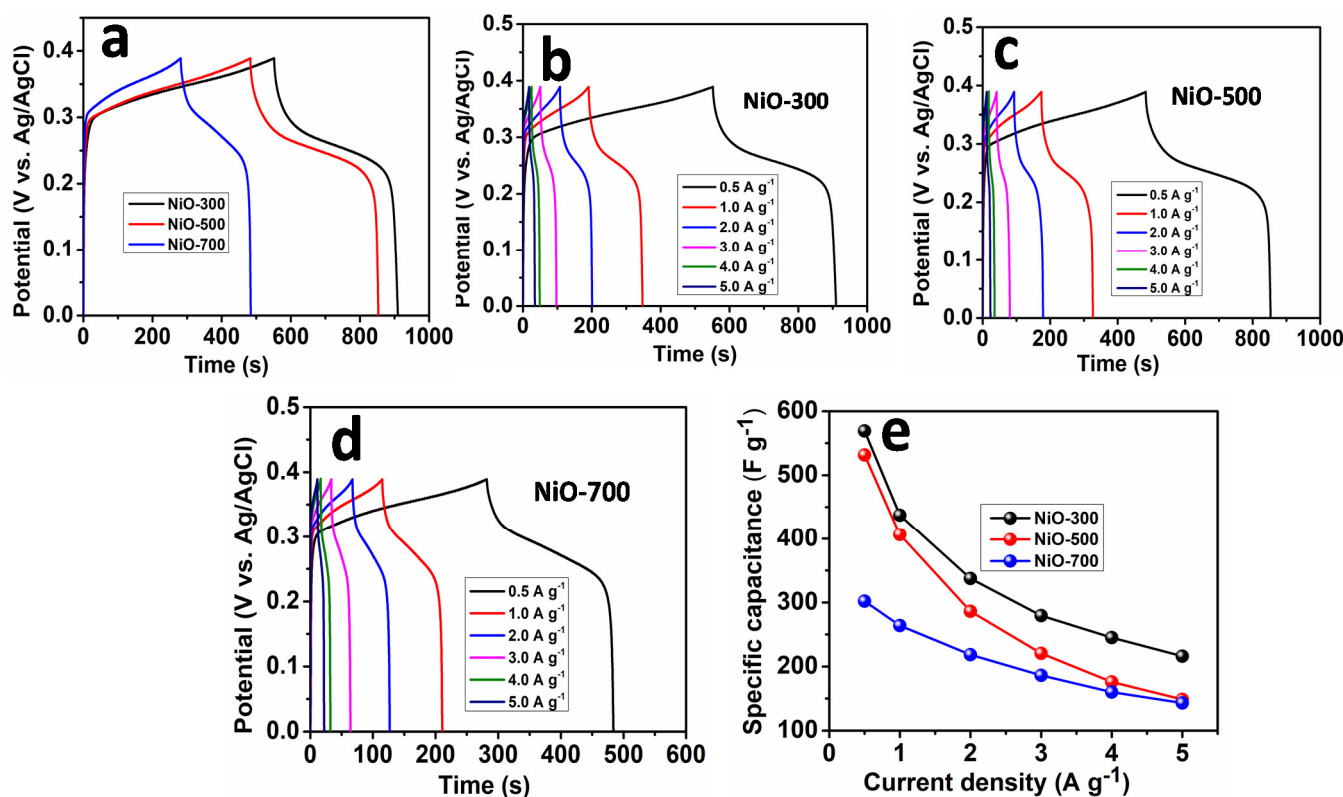


**Figure 6.** (a) Comparative GCD profiles of three different NiO electrodes; (b–d) GCD profiles of NiO-300, NiO-500, and NiO-700 at various densities of current; and (e) specific capacitances versus various current densities of NiO electrode materials.

Figure 7a–c shows the EIS (raw and fitted) data of NiO-300, NiO-500, and NiO-700 electrodes. The corresponding equivalent circuit of measured EIS were fitted with different components for example solution resistance ( $R_s$ ), charge-transfer resistance ( $R_{ct}$ ), Warburg impedance ( $Z_W$ ), double-layer capacitance ( $C_p$ ), and constant phase element ( $Q$ ) as shown in Figure 7d. The  $R_s$  was estimated from the intercepts of higher frequency region, and it was found to be 1.9, 1.4, and 1.4  $\Omega$ , respectively. The  $R_s$  values were calculated from the combination of two resistances, which are the electronic-resistance from the active substance and ionic-resistance of the electrolyte. From the semicircle, the  $R_{ct}$  was determined attained at the high-frequency region. The resultant  $R_{ct}$  values of NiO-300, NiO-500, and NiO-700 were 3.43, 10.1, and 22.4  $\Omega$ , respectively. Hence, a lesser  $R_{ct}$  value of NiO-300 signifies improved capacitance behavior. Furthermore, the achieved outcomes are more reliable with the observed Nyquist plot of the NiO electrode materials (Figure 7). In low-frequency range, the sloping line is related with the diffusion of  $K^+$  ions in the electrolyte–electrode interface. The Warburg diffusion ( $Z_W$ ), was higher in the NiO-300 electrode (5.3  $\Omega$ ) due to the porous nature providing more active sites; however, the NiO-500 (11.3  $\Omega$ ) and NiO-700 (16.8  $\Omega$ ) electrodes diffusion was reduced slightly because of the fewer active sites. The high capacitance and low resistance showed that the NiO-300 electrode is an appropriate material for ASC device applications. The major parameter for a supercapacitor is the frequency factor ( $n$ ), which can give details about the ideality of an electrode toward supercapacitive behavior. The values of  $n$  differ between 0 and 1:  $n = 0$  indicate the resistor;  $n = 1$  indicates the ideal capacitor. The NiO-300 electrodes showed moderate supercapacitor behavior and achieved the highest  $n$  value of 0.90 compared to NiO-500 and NiO-700 electrodes shows 0.76 and 0.71 respectively.

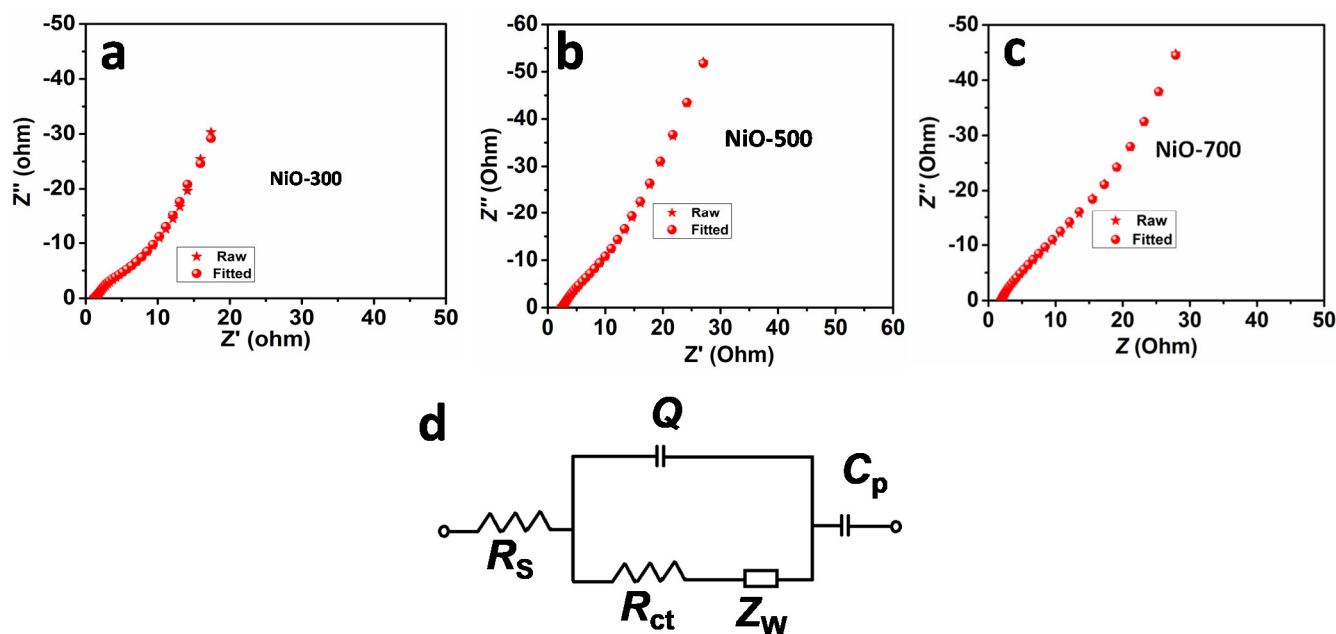
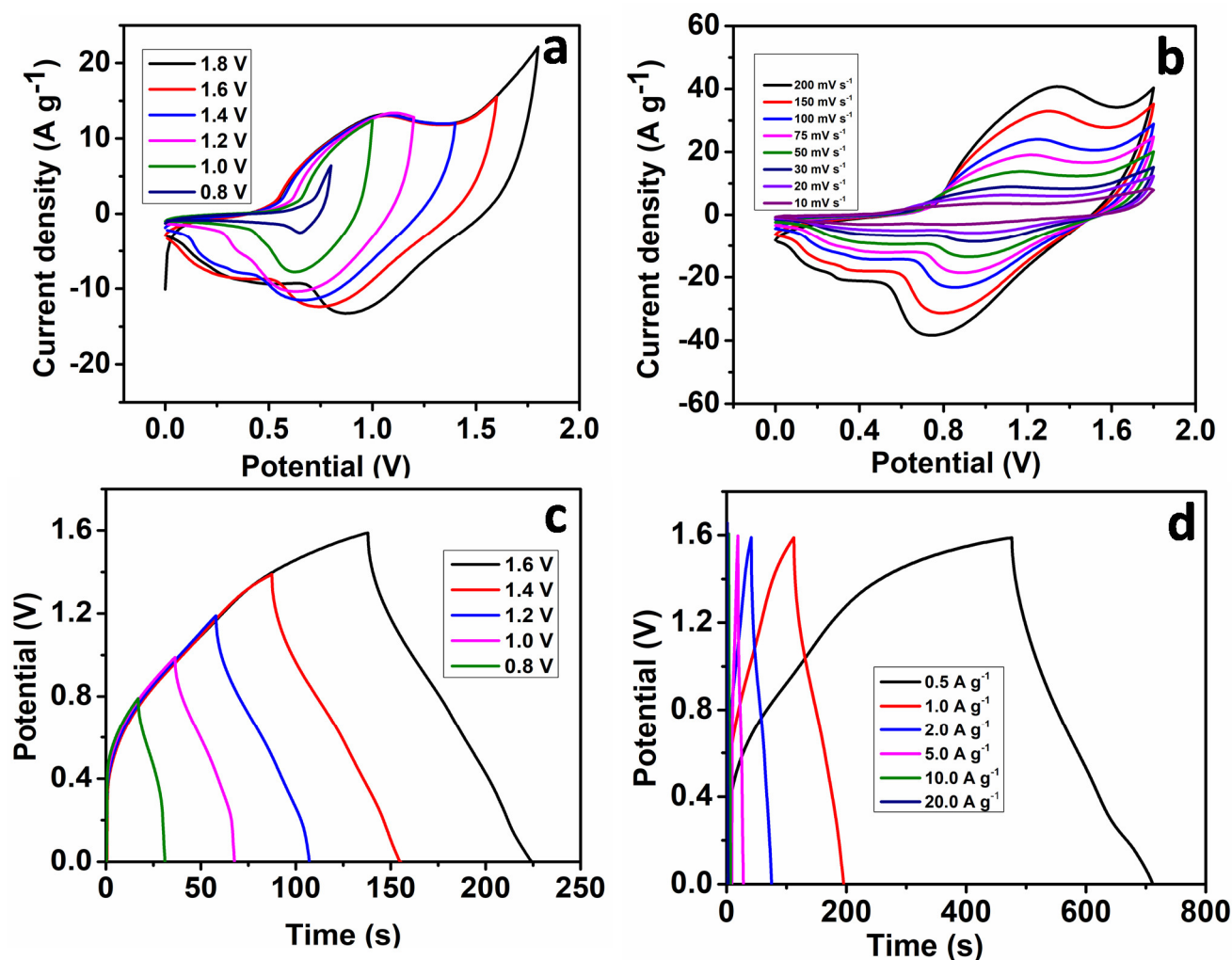


Figure 7. EIS of the (a) NiO-300, (b) NiO-500, (c) NiO-700 electrodes, and (d) equivalent circuit.

The ASC device was constructed by employing AC as the anode and NiO-300 nanoflakes as the cathode. Figure 8a presents the CV profiles of ASC device in various cut-off regions at a sweep rate of 50  $\text{mV s}^{-1}$ . From the figure, the CV profiles of ASC device exhibits typical capacitive performance with quasi-rectangular shape, which correspond to mutual contribution of the EDLC and pseudocapacitance [10]. In addition, when increasing the working cut-off region, more Faradaic electrochemical reactions were occurred. The oxygen evolution can also be noticed on the CV curve when the working potential goes beyond 1.7 V. The NiO//AC ASC device is largely dependent on the cut-off region. As a consequence, 1.6 V was chosen as the potential window region for subsequent investigation of the ASC

device electrochemical performances. Figure 8b illustrates the CV profiles of the ASC device at various scan rates in the cut-off region from 0 to 1.6 V. The current density increases as the sweep rate increases, and the oxidation peak potential shifted to a more positive potential, similar to the three-electrode device results.



**Figure 8.** (a) CV profiles of NiO//AC ASC device examined at various cut-off windows at a sweep rate of  $50 \text{ mV s}^{-1}$ , (b) CV profiles of NiO//AC ASC device at various sweep rates, (c) GCD curves of NiO//AC ASC device measured at various cut-off range at a current density of  $1 \text{ A g}^{-1}$ , and (d) GCD profiles of NiO//AC ASC device at various current densities.

Figure 8c shows the GCD profiles were measured at different cut-off regions between 0.6 and 1.6 V at  $1 \text{ A g}^{-1}$ . From the results, the device shows excellent supercapacitive performances with quasi-symmetrical triangular GCD features, even at a potential window maximum of 1.6 V, and the specific capacitance rose with increasing potential window. The excellent performances of the ASC device can be accredited to the higher specific capacitances and rate capability of the NiO nanoflakes in addition to the synergistic effects of the cathode and anode. The GCD profiles of the NiO//AC device at different current densities are presented in Figure 8d. It can be found that the shape of charge–discharge profiles are nearly symmetric, indicating that the electrochemical reactions are well reversible. The specific capacitances were estimated based on the weight of the cathode attains and discharge time  $147.5 \text{ F g}^{-1}$  at  $0.5 \text{ A g}^{-1}$  and the capacitance still shows a retention of  $30 \text{ F g}^{-1}$  at  $20 \text{ A g}^{-1}$ . Furthermore, the specific capacitance, energy density, and power density maximum and stability of the NiO//AC ASC device was lower or comparable to

the existing reports of the related metal oxides as cathode and activated carbon as anode, respectively as shown in Table 1.

**Table 1.** Comparison of the electrochemical performances of the NiO electrode and those of related metal oxide electrode materials.

Electrode	Electrolyte	Specific Capacitance	Energy Density (Wh kg <sup>-1</sup> )	Power Density (W kg <sup>-1</sup> )	Stability (Cycles/Capacitance Retention)	Ref.
Porous NiO film	1 M NaOH	104.2 F g <sup>-1</sup> @ 1 mA cm <sup>-1</sup>	—	—	5000 cycles/—	[45]
NiO core/shell	5 M KOH	448 F g <sup>-1</sup> @ 0.5 A g <sup>-1</sup>	—	—	500 cycles/—	[46]
NiO hollow spheres	2 M KOH	346 F g <sup>-1</sup> @ 1 A g <sup>-1</sup>	—	—	5000 cycles/—	[47]
NiO nanotubes	6 M KOH	266 F g <sup>-1</sup> @ 0.1 A g <sup>-1</sup>	—	—	2000 cycles/93%	[48]
NiO nanofibers	6 M KOH	336 F g <sup>-1</sup> @ 5 mA cm <sup>-1</sup>	—	—	1000 cycles/87%	[49]
NiO-carbon	6 M KOH	265 F g <sup>-1</sup> @ 0.25 A g <sup>-1</sup>	—	—	1000 cycles/70%	[50]
3D-NiO/Graphene	6 M KOH	587.3 F g <sup>-1</sup> @ 1 A g <sup>-1</sup>	—	—	1000 cycles/98.5%	[51]
NiAl-LDHs//AC	6 M KOH	959 F g <sup>-1</sup> @ 1 A g <sup>-1</sup>	21.0	700	6000 cycles/63%	[52]
NiAl-LDHs-rGO//AC	6 M KOH	129 A h kg <sup>-1</sup> @ 1 A g <sup>-1</sup>	15.4	342	10,000 cycles/72.7%	[53]
CoAl LDHCNTs//AC	2 M KOH	884 F g <sup>-1</sup> @ 0.86 A g <sup>-1</sup>	28.0	444.1	1000 cycles/68%	[54]
NiWO <sub>4</sub> //AC	2 M KOH	586.2 F g <sup>-1</sup> @ 0.5 A g <sup>-1</sup>	25.3	200	5000 cycles/91.4%	[55]
NiO nanoflakes//AC	2 M KOH	568.7F g <sup>-1</sup> @ 0.5 A g <sup>-1</sup>	52.4	32,000	5000 cycles/90.6%	[This work]

Figure 9a shows the Ragone plot of NiO//AC ASC device examined in the potential range between 0 V and 1.6 V. The NiO//AC ASC device displays high energy density of 52.4 and 10.6 Wh kg<sup>-1</sup> at a power density of 800 and 32,000 W kg<sup>-1</sup>, respectively. Finally, the cyclability of NiO//AC ASC device was investigated at 1 A g<sup>-1</sup> over 5000 cycles were performed for a potential window ranging from 0 to 1.6 V as shown in Figure 9b. The specific capacitance of the ASC device still has retention of 95.6 F g<sup>-1</sup> during 5000 GCD cycles at 1 A g<sup>-1</sup>, which is about 90.6% of the initial capacitance. The GCD profiles of the device retain the same symmetric profile after 5000 cycles, indicating that the device still has good reversible electrochemical activity. The specific capacitance is fading due to the increase in ohmic resistance of the ASC device during cycling. The interfacial contact between the active material and the substrate may deteriorate with time as a result of the active material volume changes during the charge–discharge process, resulting in a higher ohmic resistance for the device. Furthermore, the active material may come loose from the substrate during cycling, resulting in a capacitance underestimation. As a result, the electrode construction method must be optimized in order to improve the device cyclability. The realistic feasibility of the NiO//AC ASC device was studied by connecting a couple of ASC devices in series to lighten with light emitting diode and powered ~30 min, after that the devices were charged to 1.6 V for 25 s (inset of Figure 9b), thus resulting in the huge potential of this NiO//AC ASC device for next generation energy storage applications. Figure 9c,d shows the GCD profiles and CV profiles before and after stability studies (after 5000 cycles) of the ASC devices, respectively. The specific capacitance of the ASC device still has maintained ~90% of the initial capacitance after 5000 GCD cycles.

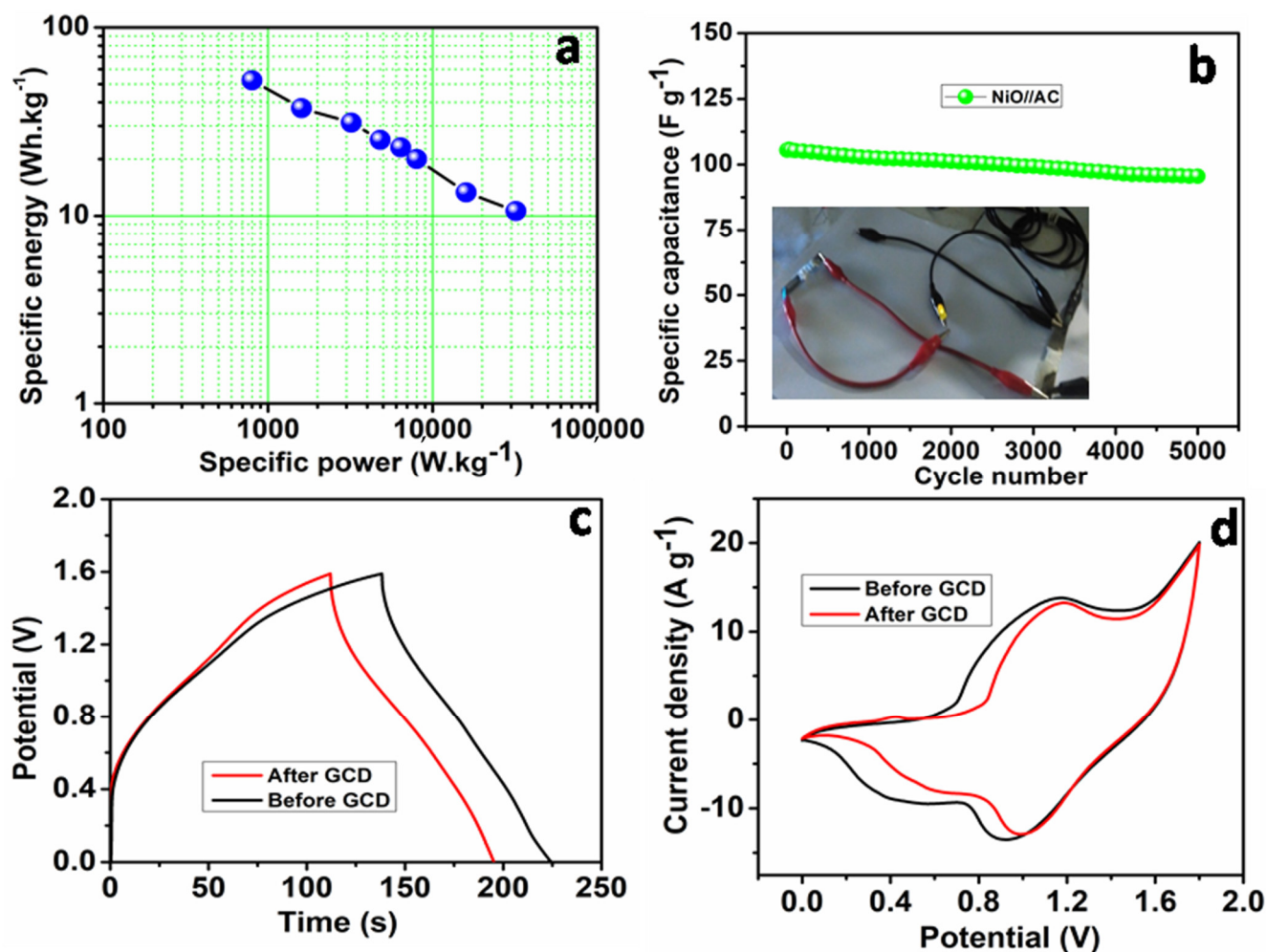


**Figure 9.** (a) Ragone plot of the assembled NiO//AC ASC device. (b) Long-term cyclability of the NiO//AC ASC device (Inset: Snapshot of light emitting diode powered by series of NiO//AC ASC devices). (c) GCD profiles of ASC device of before and after 5000 cycles. (d) CV curves of ASC device before and after the 5000th cycle of GCD measurements.

#### 4. Conclusions

In summary, we successfully demonstrate the preparation of porous NiO nanoflakes with CTAB and laboratory tissue paper as template by hydrothermal technique followed by calcination at three various temperatures (300, 500, and 700 °C). The NiO-300 electrode demonstrated high specific capacitance of  $568.7 \text{ F g}^{-1}$  at  $0.5 \text{ A g}^{-1}$  in the three-electrode system. The ASC device employed of NiO-300 as the positive electrode and activated carbon as the negative electrode shows a high capacitance of  $105 \text{ F g}^{-1}$  at  $1 \text{ A g}^{-1}$  and also demonstrated excellent cyclability. In addition, the ASC device displayed gravimetric energy density of  $52.4 \text{ Wh kg}^{-1}$  at a power density of  $800 \text{ W kg}^{-1}$ . The promising results suggest that porous NiO nanoflakes are an excellent electrode material for ultrahigh-performance supercapacitors with viable applications.

**Author Contributions:** Investigation and writing—original draft, R.V.; Investigation and visualization, R.S.B.; Conceptualization, R.A.; Validation, H.-J.K.; Project administration and supervision, M.Y.; Supervision and validation, L.M.S. and A.L.F.d.B. All authors have read and agreed to the published version of the manuscript.

**Funding:** This work was partly supported by the National Research Foundation of Korea (NRF) grant funded by the Korea government (MSIT) (No. 2021R1A4A1027087).

**Acknowledgments:** The authors gratefully acknowledge the financial support from BK21 Plus Creative Human Resource Education and Research Programs for ICT Convergence in the Fourth Industrial Revolution, Pusan National University, Busan, South Korea. R. Suresh Babu would like to thank FAPERJ for the financial support of post-doctoral senior fellowship (E-26/202.333/2021).

**Conflicts of Interest:** The authors declare no conflict of interest.

## References

1. Yang, Z.; Zhang, J.; Kintner-Meyer, M.C.W.; Lu, X.; Choi, D.; Lemmon, J.P.; Liu, J. Electrochemical Energy Storage for Green Grid. *Chem. Rev.* **2011**, *111*, 3577–3613. [[CrossRef](#)] [[PubMed](#)]
2. Yu, G.; Hu, L.; Vosgueritchian, M.; Wang, H.; Xie, X.; McDonough, J.R.; Cui, X.; Cui, Y.; Bao, Z. Solution-Processed Graphene/MnO<sub>2</sub> Nanostructured Textiles for High-Performance Electrochemical Capacitors. *Nano Lett.* **2011**, *11*, 2905–2911. [[CrossRef](#)]
3. Wang, G.; Zhang, L.; Zhang, J. A review of electrode materials for electrochemical supercapacitors. *Chem. Soc. Rev.* **2012**, *41*, 797–828. [[CrossRef](#)] [[PubMed](#)]
4. Vinodh, R.; Sasikumar, Y.; Kim, H.-J.; Atchudan, R.; Yi, M. Chitin and chitosan based biopolymer derived electrode materials for supercapacitor applications: A critical review. *J. Ind. Eng. Chem.* **2021**, *104*, 155–171. [[CrossRef](#)]
5. Kim, I.; Vinodh, R.; Gopi, C.V.V.M.; Kim, H.-J.; Babu, R.S.; Deviprasath, C.; Devendiran, M.; Kim, S. Novel porous carbon electrode derived from hypercross-linked polymer of poly(divinylbenzene-co-vinyl benzyl chloride) for supercapacitor applications. *J. Energy Storage* **2021**, *43*, 103287. [[CrossRef](#)]
6. Gopi, C.V.V.M.; Vinodh, R.; Sambasivam, S.; Obaidat, I.M.; Kim, H.-J. Recent progress of advanced energy storage materials for flexible and wearable supercapacitor: From design and development to applications. *J. Energy Storage* **2020**, *27*, 101035.
7. Vinodh, R.; Babu, R.S.; Gopi, C.V.V.M.; Deviprasath, C.; Atchudan, R.; Samyn, L.M.; De Barros, A.L.F.; Kim, H.-J.; Yi, M. Influence of annealing temperature in nitrogen doped porous carbon balls derived from hypercross-linked polymer of anthracene for supercapacitor applications. *J. Energy Storage* **2020**, *28*, 101196. [[CrossRef](#)]
8. Vinayagam, M.; Babu, R.S.; Sivasamy, A.; De Barros, A.L.F. Biomass-derived porous activated carbon from *Syzygium cumini* fruit shells and *Chrysopogon zizanioides* roots for high-energy density symmetric supercapacitors. *Biomass Bioenergy* **2020**, *143*, 105838. [[CrossRef](#)]
9. Atchudan, R.; Edison, T.N.J.I.; Perumal, S.; Vinodh, R.; Babu, R.S.; Sundramoorthy, A.K.; Renita, A.A.; Lee, Y.R. Facile synthesis of nitrogen-doped porous carbon materials using waste biomass for energy storage applications. *Chemosphere* **2022**, *289*, 133225. [[CrossRef](#)]
10. Babu, R.S.; Vinodh, R.; De Barros, A.L.F.; Samyn, L.M.; Prasanna, K.; Maier, M.A.; Alves, C.H.F.; Kim, H.-J. Asymmetric supercapacitor based on carbon nanofibers as the anode and two-dimensional copper cobalt oxide nanosheets as the cathode. *Chem. Eng. J.* **2019**, *366*, 390–403. [[CrossRef](#)]
11. Vinayagam, M.; Babu, R.S.; Sivasamy, A.; De Barros, A.L.F. Biomass-derived porous activated carbon nanofibers from *Sapindus trifoliatus* nut shells for high-performance symmetric supercapacitor applications. *Carbon Lett.* **2021**, *31*, 1133–1143. [[CrossRef](#)]
12. Lu, X.; Dou, H.; Yang, S.; Hao, L.; Zhang, L.; Shen, L.; Zhang, F.; Zhang, X. Fabrication and electrochemical capacitance of hierarchical graphene/polyaniline/carbon nanotube ternary composite film. *Electrochim. Acta* **2011**, *56*, 9224–9232. [[CrossRef](#)]
13. Feng, X.M.; Li, R.M.; Ma, Y.W.; Chen, R.F.; Shi, N.E.; Fan, Q.L.; Huang, W. One-Step Electrochemical Synthesis of Graphene/Polyaniline Composite Film and Its Applications. *Adv. Funct. Mater.* **2011**, *21*, 2989–2996. [[CrossRef](#)]
14. Song, C.-S.; Gopi, C.V.V.M.; Vinodh, R.; Sambasivam, S.; Kalla, R.M.N.; Obaidat, I.M.; Kim, H.-J. Morphology-dependent binder-free CuNiO<sub>2</sub> electrode material with excellent electrochemical performances for supercapacitors. *J. Energy Storage* **2019**, *26*, 101037. [[CrossRef](#)]
15. Gopi, C.V.V.M.; Sambasivam, S.; Vinodh, R.; Kim, H.-J.; Obaidat, I.M. Nanostructured Ni-doped CuS thin film as an efficient counter electrode material for high-performance quantum dot-sensitized solar cells. *J. Mater. Sci. Mater. Electron.* **2020**, *31*, 975–982. [[CrossRef](#)]
16. Park, T.Y.; Gopi, C.V.V.M.; Vinodh, R.; Kim, H.-J. Facile synthesis of highly efficient V<sub>2</sub>O<sub>5</sub>@NiCo<sub>2</sub>O<sub>4</sub> as battery-type electrode material for high-performance electrochemical supercapacitors. *J. Mater. Sci. Mater. Electron.* **2019**, *30*, 13519–13524. [[CrossRef](#)]
17. Maier, M.A.; Babu, R.S.; Sampaio, D.M.; De Barros, A.L.F. Binder-free polyaniline interconnected metal hexacyanoferrates nanocomposites (Metal = Ni, Co) on carbon fibers for flexible supercapacitors. *J. Mater. Sci. Mater. Electron.* **2017**, *28*, 17405–17413. [[CrossRef](#)]
18. Babu, R.S.; De Barros, A.L.F.; Maier, M.A.; Sampaio, D.M.; Balamurugan, J.; Lee, J.H. Novel polyaniline/manganese hexacyanoferrate nanoparticles on carbon fiber as binder-free electrode for flexible supercapacitors. *Compos. Part B Eng.* **2018**, *143*, 141–147. [[CrossRef](#)]
19. Samyn, L.M.; Babu, R.S.; Devendiran, M.; De Barros, A.L.F. Electropolymerization of p-phenylenediamine films on carbon fiber fabrics electrode for flexible supercapacitors: Surface and electrochemical characterizations. *Ionics* **2020**, *26*, 3041–3050. [[CrossRef](#)]

20. Samyn, L.M.; Babu, R.S.; Devendiran, M.; De Barros, A.L.F. One-step electropolymerization of methylene blue films on highly flexible carbon fiber electrode as supercapacitors. *Micro Nano Syst. Lett.* **2021**, *9*, 1–10. [[CrossRef](#)]
21. Santos, R.S.; Babu, R.S.; Devendiran, M.; Haddad, D.B.; De Barros, A.L.F. Facile synthesis of transition metal (M = Cu, Co) oxide grafted graphitic carbon nitride nanosheets for high performance asymmetric supercapacitors. *Mater. Lett.* **2022**, *308*, 131156. [[CrossRef](#)]
22. Thalji, M.R.; Ali, G.A.M.; Liu, P.; Zhong, Y.L.; Chong, K.F.  $W_{18}O_{49}$  nanowires-graphene nanocomposite for asymmetric supercapacitors employing  $AlCl_3$  aqueous electrolyte. *Chem. Eng. J.* **2021**, *409*, 128216. [[CrossRef](#)]
23. Oh, S.H.; Nazar, L.F. Direct synthesis of electroactive mesoporous hydrous crystalline  $RuO_2$  templated by a cationic surfactant. *J. Mater. Chem.* **2010**, *20*, 3834–3839. [[CrossRef](#)]
24. Ye, J.-S.; Cui, H.F.; Liu, X.; Lim, T.M.; Zhang, W.-D.; Sheu, F.-S. Preparation and characterization of aligned carbon nanotubes-ruthenium oxide nanocomposites for supercapacitors. *Small* **2005**, *1*, 560–565. [[CrossRef](#)]
25. Li, Y.; Huang, K.; Liu, S.; Yao, Z.; Zhuang, S. Meso-macroporous  $Co_3O_4$  electrode prepared by polystyrene spheres and carbowax templates for supercapacitors. *J. Solid State Electrochem.* **2011**, *15*, 587–592. [[CrossRef](#)]
26. Xu, M.-W.; Zhao, D.-D.; Bao, S.-J.; Li, H.-L. Mesoporous amorphous  $MnO_2$  as electrode material for supercapacitor. *J. Solid State Electrochem.* **2007**, *11*, 1101–1107. [[CrossRef](#)]
27. Yang, Y.Y.; Hu, Z.A.; Zhang, Z.Y.; Zhang, F.H.; Zhang, Y.J.; Liang, P.J.; Zhang, H.Y.; Wu, H.Y. Reduced graphene oxide–nickel oxide composites with high electrochemical capacitive performance. *Mater. Chem. Phys.* **2012**, *133*, 363–368. [[CrossRef](#)]
28. Zhao, B.; Song, J.; Liu, P.; Xu, W.; Fang, T.; Jiao, Z.; Zhang, H.; Jiang, Y. Monolayer graphene/ $NiO$  nanosheets with two-dimension structure for supercapacitors. *J. Mater. Chem.* **2011**, *21*, 18792–18798. [[CrossRef](#)]
29. Ge, C.; Hou, Z.; He, B.; Zeng, F.; Cao, J.; Liu, Y.; Kuang, Y. Three-dimensional flowerlike nickel oxide supported on graphene sheets as electrode material for supercapacitors. *J. Sol-Gel Sci. Technol.* **2012**, *63*, 146–152. [[CrossRef](#)]
30. Fan, L.; Tang, L.; Gong, H.; Yao, Z.; Guo, R. Carbon–nanoparticles encapsulated in hollow nickel oxides for supercapacitor application. *J. Mater. Chem.* **2012**, *22*, 16376–16381. [[CrossRef](#)]
31. Liu, K.; Zhang, Y.; Zhang, W.; Zheng, H.; Su, G. Charge-discharge process of  $MnO_2$  supercapacitor. *Trans. Nonferr. Met. Soc. China* **2007**, *17*, 649–653. [[CrossRef](#)]
32. Brousse, T.; Toupin, M.; Dugas, R.; Athouel, L.; Crosnier, O.; Belanger, D. Crystalline  $MnO_2$  as possible alternatives to amorphous compounds in electrochemical supercapacitors. *J. Electrochem. Soc.* **2006**, *153*, A2171–A2180. [[CrossRef](#)]
33. Wang, Y.; Xia, Y. Electrochemical capacitance characterization of  $NiO$  with ordered mesoporous structure synthesized by template SBA-15. *Electrochim. Acta* **2006**, *51*, 3223–3227. [[CrossRef](#)]
34. Lang, J.-W.; Kong, L.-B.; Wu, W.-J.; Luo, Y.-C.; Kang, L. Facile approach to prepare loose-packed  $NiO$  nano-flakes materials for supercapacitors. *Chem. Commun.* **2008**, *35*, 4213–4215. [[CrossRef](#)] [[PubMed](#)]
35. Liu, H.; Wang, G.; Liu, J.; Qiao, S.; Ahn, H. Highly ordered mesoporous  $NiO$  anode material for lithium ion batteries with an excellent electrochemical performance. *J. Mater. Chem.* **2011**, *21*, 3046–3052. [[CrossRef](#)]
36. Wang, X.; Li, L.; Zhang, Y.; Wang, S.; Zhang, Z.; Fei, L.; Qian, Y. High-yield synthesis of  $NiO$  nanoplatelets and their excellent electrochemical performance. *Cryst. Growth Des.* **2006**, *6*, 2163–2165. [[CrossRef](#)]
37. Justin, P.; Meher, S.K.; Rao, G.R. Tuning of capacitance behavior of  $NiO$  using anionic, cationic, and nonionic surfactants by hydrothermal synthesis. *J. Phys. Chem. C* **2010**, *114*, 5203–5210. [[CrossRef](#)]
38. Gopi, C.V.V.M.; Vinodh, R.; Sambasivam, S.; Obaidat, I.M.; Singh, S.; Kim, H.-J.  $Co_9S_8-Ni_3S_2/CuMn_2O_4-NiMn_2O_4$  and  $MnFe_2O_4-ZnFe_2O_4$ /graphene as binder-free cathode and anode materials for high energy density supercapacitors. *Chem. Eng. J.* **2020**, *381*, 122640. [[CrossRef](#)]
39. Vinodh, R.; Gopi, C.V.V.M.; Kummara, V.G.R.; Atchudan, R.; Ahamad, T.; Sambasivam, S.; Yi, M.; Obaidat, I.M.; Kim, H.-J. A review on porous carbon electrode material derived from hypercross-linked polymers for supercapacitor applications. *J. Energy Storage* **2020**, *32*, 101831. [[CrossRef](#)]
40. Wardani, M.; Yulizar, Y.; Abdullah, I.; Apriandanu, D.O.B. Synthesis of  $NiO$  nanoparticles via green route using *Ageratum conyzoides* L. leaf extract and their catalytic activity. *IOP Conf. Ser. Mater. Sci. Eng.* **2019**, *509*, 012077. [[CrossRef](#)]
41. Shen, L.; Che, Q.; Li, H.; Zhang, X. Mesoporous  $NiCo_2O_4$  nanowire arrays grown on carbon textiles as binder-free flexible electrodes for energy storage. *Adv. Funct. Mater.* **2014**, *24*, 2630–2637. [[CrossRef](#)]
42. Santhoshkumar, P.; Prasanna, K.; Jo, Y.N.; Sivagami, I.N.; Kang, S.H.; Lee, C.W. Hierarchically structured mesoporous bimetallic oxides as a potential anode material for rechargeable lithium batteries. *J. Alloys Compd.* **2019**, *771*, 555–564. [[CrossRef](#)]
43. Jahromi, S.P.; Pandikumar, A.; Goh, B.T.; Lim, Y.S.; Basirun, W.J.; Lim, H.N.; Huang, N.M. Influence of particle size on performance of a nickel oxide nanoparticle-based supercapacitor. *RSC Adv.* **2015**, *5*, 14010–14019. [[CrossRef](#)]
44. Babu, R.S.; Prabhu, P.; Narayanan, S.S. Green synthesized nickel nanoparticles modified electrode in ionic liquid medium and its application towards determination of biomolecules. *Talanta* **2013**, *110*, 135–143. [[CrossRef](#)] [[PubMed](#)]
45. Inamdar, A.I.; Kim, Y.; Pawar, S.M.; Kim, J.H.; Im, H.; Kim, H. Chemically grown, porous, nickel oxide thin-film for electrochemical supercapacitors. *J. Power Sources* **2011**, *196*, 2393–2397. [[CrossRef](#)]
46. Han, D.; Xu, P.; Jing, X.; Wang, J.; Song, D.; Liu, J.; Zhang, M. Facile approach to prepare hollow core-shell  $NiO$  microspheres for supercapacitor electrodes. *J. Solid State Chem.* **2013**, *203*, 60–67. [[CrossRef](#)]
47. Yan, X.; Tong, X.; Wang, J.; Gong, C.; Zhang, M.; Liang, L. Rational synthesis of hierarchically porous  $NiO$  hollow spheres and their supercapacitor application. *Mater. Lett.* **2013**, *95*, 1–4. [[CrossRef](#)]

48. Xu, J.; Gao, L.; Cao, J.; Wang, W.; Chen, Z. Electrochemical capacitance of nickel oxide nanotubes synthesized in anodic aluminum oxide templates. *J. Solid State Electrochem.* **2010**, *15*, 2005–2011. [[CrossRef](#)]
49. Ren, B.; Fan, M.; Liu, Q.; Wang, J.; Song, D.; Bai, X. Hollow NiO nanofibers modified by citric acid and the performances as supercapacitor electrode. *Electrochim. Acta* **2013**, *92*, 197–204. [[CrossRef](#)]
50. Wang, Y.; Xing, S.; Zhang, E.; Wei, J.; Suo, H.; Zhao, C.; Zhao, X. One-pot synthesis of nickel oxide–carbon composite microspheres on nickel foam for supercapacitors. *J. Mater. Sci.* **2011**, *47*, 2182–2187. [[CrossRef](#)]
51. Chen, W.; Gui, D.; Liu, J. Nickel oxide/graphene aerogel nanocomposite as a supercapacitor electrode material with extremely wide working potential window. *Electrochim. Acta* **2014**, *222*, 1424–1429. [[CrossRef](#)]
52. Zhang, L.; Yao, H.; Li, Z.; Sun, P.; Liu, F.; Dong, C.; Wang, J.; Li, Z.; Wu, M.; Zhang, C.; et al. Synthesis of delaminated layered double hydroxides and their assembly with graphene oxide for supercapacitor application. *J. Alloys Compd.* **2017**, *711*, 31–41. [[CrossRef](#)]
53. Ge, X.; Gu, C.; Yin, Z.; Wang, X.; Tu, J.; Li, J. Periodic stacking of 2D charged sheets: Self-assembled superlattice of Ni-Al layered double hydroxide (LDH) and reduced graphene oxide. *Nano Energy* **2016**, *20*, 185–193. [[CrossRef](#)]
54. Yu, L.; Shi, N.; Liu, Q.; Wang, J.; Yang, B.; Wang, B.; Yan, H.; Sun, Y.; Jing, X. Facile synthesis of exfoliated Co-Al LDH-carbon nanotube composites with high performance as supercapacitor electrodes. *Phys. Chem. Chem. Phys.* **2014**, *16*, 17936–17942. [[CrossRef](#)] [[PubMed](#)]
55. Niu, L.; Li, Z.; Xu, Y.; Sun, J.; Hong, W.; Liu, X.; Wang, J.; Yang, S. Simple synthesis of amorphous NiWO<sub>4</sub> nanostructure and its application as a novel cathode material for asymmetric supercapacitors. *ACS Appl. Mater. Interfaces* **2013**, *5*, 8044–8052. [[CrossRef](#)] [[PubMed](#)]